Supplementary Material

"Formation of sea ice ponds from ice-shelf runoff, adjacent to the McMurdo Ice Shelf, Antarctica"

Grant J. Macdonald, Predrag Popović and David P. Mayer

Satellite Imagery Analysis

We downloaded all November-February Landsat 8 Operational Land Imager (OLI) and Sentinel-2A and 2B images of the study region that were sufficiently cloud-free over features of interest were downloaded, covering the period 29 November 2015 to 24 January 2019. Sentinel-2B only launched in March 2017, during the study period. Images with heavy cloud cover could be used for analysis provided that at least one of our sites of interest was visible. We chose Landsat 8 and Sentinel-2, as opposed to Moderate Resolution Imaging Spectroradiometer (MODIS), because these instruments have relatively high spatial resolutions. Landsat 8 imagery has a spatial resolution of 30 m, or 15 m when pan-sharpened, and Sentinel-2 has a spatial resolution of 10 m. MODIS, in contrast, has a resolution of 250 m, which is inadequate for resolving the presence or character of many of the ponds of interest in this study.

All true-colour pan-sharpened Landsat and true-colour Sentinel images were cropped to an area encompassing the region of interest and some surrounding area (Fig. 1) and assembled into the time-series used to create Video S1. Analysis was carried out using a combination of manual visual interpretation of the time-series, and analysis quantification of ponded area. There is not a reliable automated way to determine certain nuanced elements of the evolution of ponds, or for example, whether a pond freezes-over or drains. While there is the potential for error in manual visual interpretation, given our knowledge and experience of the ice in the area from previous studies and time spent there in 2015-2016 and 2016-2017 (for fieldwork for other studies; Banwell and others; 2017; MacAyeal and others, 2018; Banwell and others, 2019; Macdonald and others, 2019; MacAyeal and others, *in press*), we consider manual visual interpretation optimal for elements of our analysis.

Ponded-area calculations

To calculate ponded area, we first determined which images had sea ice ponds present on the sea ice adjacent to the McMurdo Ice Shelf using manual visual interpretation of true-colour images. If we determined that there were no ponds, either because none had developed yet or because they had frozen over, we assigned a value of 0 to pond area. If we determined that meltwater was present on a particular day, and the image was cloud-free over the study area (Fig. 1), we processed the images for pond-area quantification. If on a particular day there was both a Sentinel-2 and Landsat 8 image available, we used the Sentinel-2 image because they have a higher spatial resolution.

To process the images for pond-area quantification, we selected the blue and red bands of each image. For Landsat 8, we used band 2 (blue, 450-510 nm) and band 4 (red, 640-670 nm) and for Sentinel 2, we also used band 2 (blue, 459-525 nm) and band 4 (red, 649-680 nm). We then cropped each image to the study area (Fig. 1) using Extract by Mask in ArcMap™.

For the Landsat 8 images, we then used image's metadata to convert digital numbers to top-of-atmosphere (TOA) reflectance and to correct for solar elevation. For the Sentinel-2 images, we used the L1C product which has already been processed to TOA reflectance. These TOA reflectance values represent an adequate proxy for surface reflectance for our purposes (Pope and others, 2016).

To identify water-covered pixels, we calculated the normalized difference water index adapted for ice ($NDWI_{ice}$), defined as

$$NDWI_{ice} = B2 - B4 / (B2 + B4)$$

where B2 and B4 represent the blue and red bands, respectively. We determined a threshold $NDWI_{ice}$ value by testing different values and comparing the results to our manual visual interpretation of the images. Pixels with an $NDWI_{ice}$ value above this value were assigned as water-covered. For Landsat 8 images, pixels with $NDWI_{ice} > 0.12$ were assigned as water-covered. This threshold value has been used to detect water-covered pixels in Landsat 8 in other studies on glaciers and ice shelves (e.g. Yang and Smith, 2013; Bell and others, 2017). For Sentinel-2 images, we found a lower threshold value of $NDWI_{ice} > 0.09$ to be most suitable.

Following previous studies of ponds on glaciers and ice shelves (Pope and others, 2016; Macdonald and others, 2018), we then excluded ponds that were identified as having an area of ≤ 4 pixels. We deemed that a threshold of 4 was sufficiently high to exclude small ponds that consisted exclusively of mixed pixels (i.e. pixels with a value representative of the average of different surface types e.g. snow/ice/water), while being sufficiently low to maximize the inclusion of small lakes. This meant that the smallest detectable pond area was 0.0036 km^2 for Landsat 8 images, and 0.0004 km^2 for Sentinel 2 images.

Differences in the spatial resolution, and radiometric differences between the bands, of the two satellite instruments will be responsible for some differences in the calculated areas between images.

Grant Macdonald

Supplementary Figures

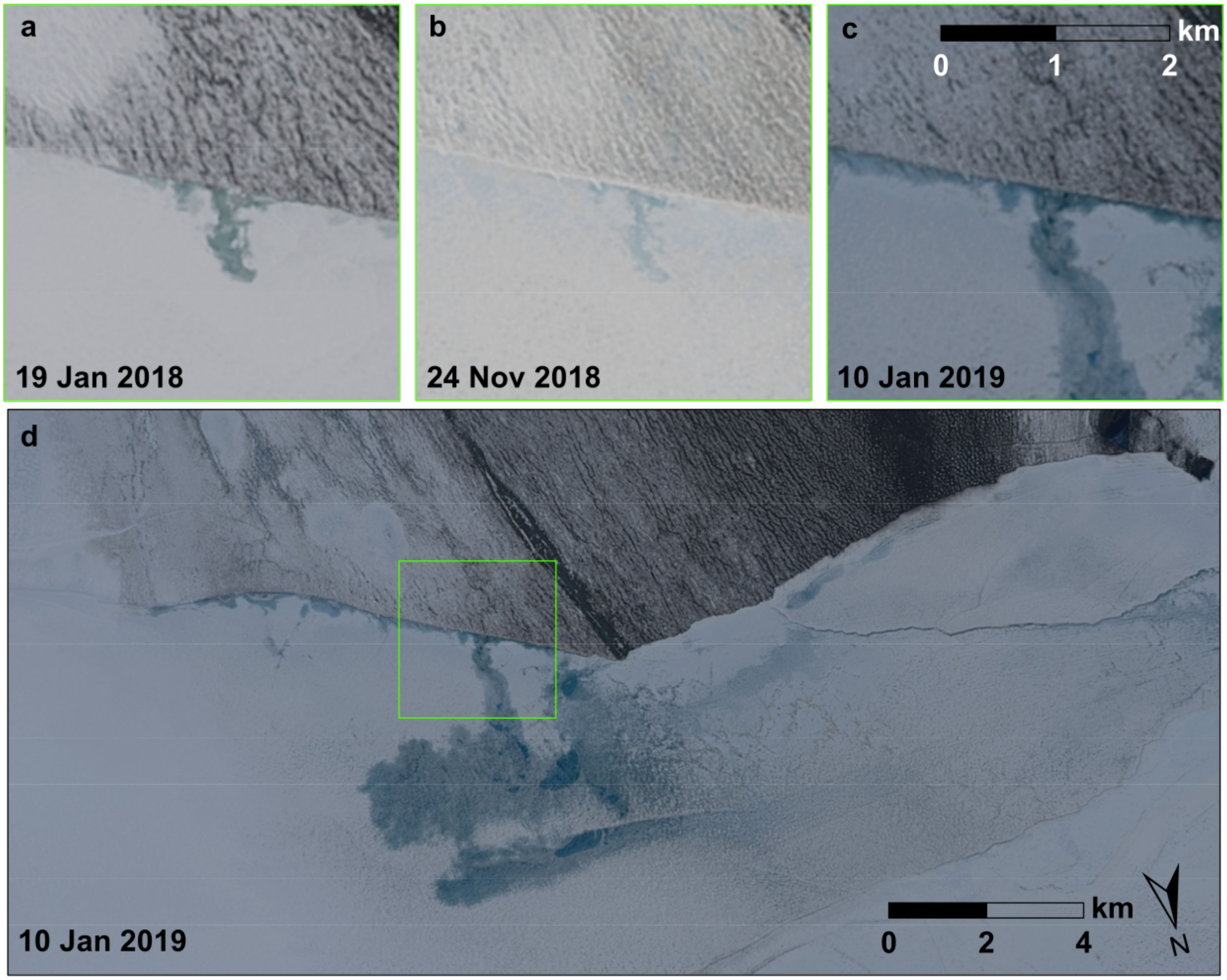

Fig. S1: A pond that (a) forms and freezes over in the 2017-2018 austral summer (b) persists as a feature into the following summer, when a pond forms at the same site in the same approximate form. (c) In the 2018-2019 season, ponding expands away from the ice-shelf front at this site. The extent of (d) is the same as the study site shown in Fig. 1 by the yellow box, and the green box in (d) shows the extent of (a-c).

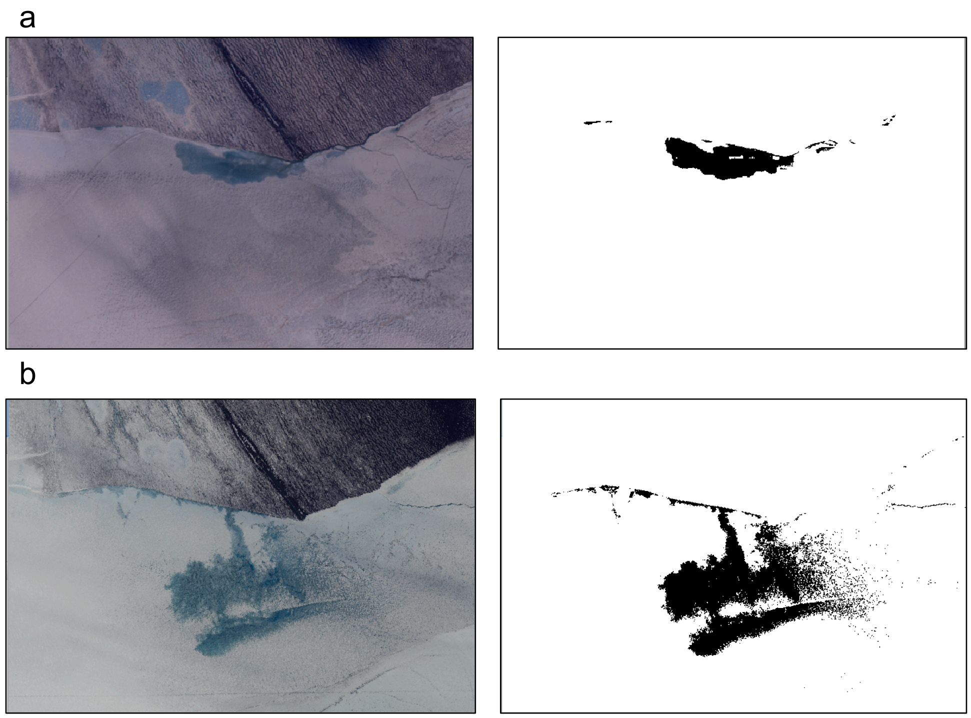

Fig. S2: Comparisons of true colour satellite images (left) and ponds identified using the $NDWI_{ice}$ method with that image (right). Pixels on the sea ice that are identified as being water-covered are black in the right image. (a) is a Landsat 8 image from 4 December 2015 and a $NDWI_{ice}$ threshold of > 0.12 was used. (b) is a Sentinel-2 image from 14 January 2019 and a $NDWI_{ice}$ threshold of > 0.09 was used.

Video S1 (attached)**:** The complete time-series of images from 29 November 2015 to 18 February 2019

Supplementary tables

Date	Sensor	Image ID
29 November 2015	Landsat 8 OLI	LC82241282015333LGN01
01 December 2015	Landsat 8 OLI	LC80531162015335LGN01
04 December 2015	Landsat 8 OLI	LC82271282015338LGN01
15 December 2015	Landsat 8 OLI	LC80551162015349LGN01
05 January 2016	Landsat 8 OLI	LC82271282016005LGN02
14 January 2016	Sentinel 2A	S2A_OPER_PRD_MSIL1C_PDMC_20160330T074715_R085_V20160114T203520_20160114T203520.SAFE
23 January 2016	Landsat 8 OLI	LC80561152016023LGN01
01 February 2016	Landsat 8 OLI	LC80551162016032LGN01
29 November 2016	Landsat 8 OLI	LC82261282016334LGN01
03 December 2016	Landsat 8 OLI	LC80531162016338LGN01
09 December 2016	Sentinel 2A	S2A_MSIL1C_20161209T203522_N0204_R085_T58CEU_20161209T203516.SAFE
12 December 2016	Sentinel 2A	S2A_MSIL1C_20161212T204512_N0204_R128_T58CEU_20161212T204514.SAFE
13 December 2016	Sentinel 2A	S2A_MSIL1C_20161213T201532_N0204_R142_T58CEU_20161213T201529.SAFE
24 December 2016	Landsat 8 OLI	LC80561152016359LGN01
02 January 2017	Sentinel 2A	S2A_MSIL1C_20170102T201522_N0204_R142_T58CEU_20170102T201525.SAFE
11 January 2017	Landsat 8 OLI	LC82231282017011LGN01
18 January 2017	Sentinel 2A	S2A_MSIL1C_20170118T203511_N0204_R085_T58CEU_20170118T203509.SAFE
25 January 2017	Sentinel 2A	S2A_MSIL1C_20170125T202521_N0204_R042_T58CEU_20170125T202517.SAFE
28 January 2017	Sentinel 2A	S2A_MSIL1C_20170128T203511_N0204_R085_T58CEU_20170128T203513.SAFE
31 January 2017	Sentinel 2A	S2A_MSIL1C_20170131T204511_N0204_R128_T58CEU_20170131T204617.SAFE
05 February 2017	Sentinel 2A	S2A_MSIL1C_20170205T195521_N0204_R056_T58CEU_20170205T195519.SAFE
11 February 2017	Sentinel 2A	S2A_MSIL1C_20170211T201531_N0204_R142_T58CEU_20170211T201525.SAFE
14 February 2017	Sentinel 2A	S2A_MSIL1C_20170214T202521_N0204_R042_T58CEU_20170214T202519.SAFE
04 November 2017	Landsat 8 OLI	LC80531162017308LGN00
13 November 2017	Landsat 8 OLI	LC80521162017317LGN00
25 November 2017	Landsat 8 OLI	LC80561152017329LGN00
27 November 2017	Landsat 8 OLI	LC80541162017331LGN00
29 November 2017	Landsat 8 OLI	LC80521162017333LGN00
02 December 2017	Landsat 8 OLI	LC80571152017336LGN00
15 December 2017	Landsat 8 OLI	LC80521162017349LGN00
07 January 2018	Landsat 8 OLI	LC80531162018007LGN00
13 January 2018	Sentinel 2A	S2A_MSIL1C_20180113T203621_N0206_R085_T58CEU_20180113T215509.SAFE
19 January 2018	Landsat 8 OLI	LC80571152018019LGN00
12 February 2018	Sentinel 2A	S2A_MSIL1C_20180212T203621_N0206_R085_T58CEU_20180212T232245.SAFE
24 November 2018	Sentinel 2B	S2B_MSIL1C_20181124T203629_N0207_R085_T58CEU_20181124T212417.SAFE
25 November 2018	Sentinel 2B	S2B_MSIL1C_20181125T200529_N0207_R099_T58CEU_20181125T210826.SAFE
26 November 2018	Landsat 8 OLI	LC82271282018330LGN00
30 November 2018	Landsat 8 OLI	LC80541162018334LGN00
02 December 2018	Landsat 8 OLI	LC80521162018336LGN00
05 December 2018	Sentinel 2B	S2B_MSIL1C_20181205T200529_N0207_R099_T58CEU_20181205T223759.SAFE
11 December 2018	Landsat 8 OLI	LC80511162018345LGN00
16 December 2018	Landsat 8 OLI	LC82231282018350LGN00
21 December 2018	Landsat 8 OLI	LC80571152018355LGN00
04 January 2019	Sentinel 2B	S2B_MSIL1C_20190104T200529_N0207_R099_T58CEU_20190104T210616.SAFE
10 January 2019	Landsat 8 OLI	LC82221292019010LGN00
14 January 2019	Sentinel 2B	S2B_MSIL1C_20190114T200529_N0207_R099_T58CEU_20190114T211558.SAFE
15 January 2019	Landsat 8 OLI	LC80561152019015LGN00
23 January 2019	Sentinel 2B	S2B_MSIL1C_20190123T203629_N0207_R085_T58CEU_20190123T212532
24 January 2019	Sentinel 2B	LC80551162019024LGN00
13 February 2019	Sentinel 2B	S2B_MSIL1C_20190213T200529_N0207_R099_T58CEU_20190213T223839.SAFE
16 February 2019	Landsat 8 OLI	LC80561162019047LGN00

Table S1: Table of satellite image IDs and dates used to compile the time-series used for analysis

Supplementary references

Pope, A and 6 others (2016) Estimating supraglacial lake depth in West Greenland using Landsat 8 and comparison with other multispectral methods. *Cryosphere*, **10**(1), 15–27 (doi: 10.5194/tc-10-15-2016)

Yang, K. & L. C. Smith (2013) Supraglacial streams on the Greenland Ice Sheet delineated from combined spectral-shape information in high-resolution satellite imagery. *IEEE Geosci. Remote Sens. Lett.* **10**, 801–805 (doi: 10.1109/LGRS.2012.2224316)